



Investigation of Magneto Hydrodynamic Natural Convection Flows in a 3-D Rectangular Enclosure

K. N. Mohamed^{1†}, S. Benissaad², F. Berrahil² and K. Talbi²

¹Ecole Normal Supérieure d'Enseignement Technologique ENSET-Skikda. Azzaba. Alger.

²Université Mentouri Constantine faculté des sciences de l'ingénieur département de Génie mécanique.

†Corresponding Author Email: Kherief2006@yahoo.fr

(Received January 12, 2015; accepted August 29, 2015)

ABSTRACT

The article deals with magnetic field of free convective flows in cavities similar to those used in artificial growth of single crystals from melts (horizontal Bridgman configurations) and having aspect ratios an equal to "4". The combined effect of wall electrical conductivity and vertical direction of the magnetic field on the buoyancy induced flow of mercury was investigated numerically. The validation of the numerical method was achieved by comparison with both experimental and analytical data found in the literature. The plotted results for variation of velocity, temperature and Nusselt number in terms of the Hartmann number Ha and Rayleigh number "Ra" showed a considerable decrease in convection intensity as the magnetic field is increased, especially for values of "Gr" situated around 10^7 . The calculations also showed that the vertically directed magnetic field (perpendicular to the x-z plane) is the most effective in controlling the flow and hence the speed of growth of the crystal. Also, wall electrical conductivity enhances damping by changing the distribution of the induced electric current to one which augments the magnitude of the Lorentz force.

Keywords: Natural convection; Magnetic field; Cavity; Liquid metal; finite-volume; Lorentz force; tri-dimensional.

NOMENCLATURE

A	aspect ratio	R_m	Reynolds magnétique number
At	thermal diffusivity	T	temperature
B	magnetic field	T_H	hot temperature
B_0	uniform magnetic flux density	T_C	cold temperature
e_B	unitary vector of the direction of B	U	velocity in the x-direction
F_x	lorentz force in the x-direction	U	dimensionless velocity in the x-direction,
F_y	lorentz force in the y-direction	V	velocity in the y-direction
F_z	lorentz force in the z-direction	V	dimensionless velocity in the y-direction
G	gravitational acceleration	w	velocity in the z-direction
Gr	Grashof number = $g\beta(T_H - T_C)H^3/\nu^2$	W	dimensionless velocity in the z-direction
H	height of the cavity	β	thermal expansion coefficient
Ha	Hartmann number = $B_0 H \sqrt{\sigma/\rho\nu}$	ϕ	dimensionless electric potential
L	length of the enclosure	θ	dimensionless temperature
J_x	electric current in the x-direction	ρ	density of the fluid
J_y	electric current in the y-direction	σ	electrical conductivity
J_z	electric current in the z-direction	ν	kinematic viscosity of the fluid
δ_H	dimensionless thickness Hartmann layer	Plane PT	plane (y-z)
δ_S	dimensionless thickness side layer	Plane PV	plane (x-y)
Nu	average Nusselt number	Plane PH	plane (x-z)
N_x	nodes number in the x-direction	Lines CC	mid-plane (x-y)
N_y	nodes number in the y-direction	Lines AA	mid-plane (x-z)
N_z	nodes number in the z-direction	Lines BB	mid-plane (y-z)
P	pressure		
Pr	Prandtl number		
Ra	Rayleigh number		

1. INTRODUCTION

Sidewall convection in liquid metals is an important problem in the semiconductor crystal growing process known as the Bridgman technique. In this a crucible of molten material is slowly drawn from a furnace and solidification takes place. This technique is of significant practical importance in the growth of high-quality materials for optoelectronic applications as reviewed by Hill (1998). The industrial process may involve dendrite growth and the distribution of dopants and is thus a complicated problem. However, insights can be gained from studying the basic fluid dynamics that result from the differential heating of the sample since other processes are strongly influenced by the induced motion. For small temperature differences, the convection is steady and primarily consists of a large, single circulation. The bulk flow in a confined cavity evolves considerably for larger values of the driving force, as the interaction between the different regions of flow becomes significant. Thus, the mechanisms underlying the transitions to time-dependent and eventually turbulent flow are often complex.

With the application of an external magnetic field, it is possible to act on the flows without any physical contact, and thus to remove the fluctuations to control heat and mass transfers, in order to improve the quality of the crystal. For this purpose, the damping magnetic to control the flow induced by a temperature variation was used in several industrial applications. Tagawa and Ozoe (1997) numerically studied three-dimensional natural convection of a liquid metal in a cubic enclosure, under the action of a magnetic field applied, according to the three main directions. Benhadid and Henry (1997) studied the effect of a magnetic field on the flow of liquid metal in a parallelepiped cavity, using a spectral numerical method. Bessaih *et al.* (1999) numerically examined the effect of the electric conductivity of the walls and the direction of the magnetic field on the flow of Gallium. Their results show a considerable reduction in the intensity of the convection when the magnetic field increases. Juel *et al.* (1999) had the results of a numerical and experimental study of the effect of the application of a magnetic field in the direction perpendicular to the convective flow of Gallium. Aleksandrova and Molokov (2004) considered three-dimensional convection in a rectangular cavity subjected to a horizontal temperature gradient and a magnetic field, by an asymptotic model. The effectiveness of the application of the magnetic field depends considerably on the specter ratio and the value of the Hartmann number. Hof *et al.* (2005) presented an experimental study of the effect of the magnetic field on the natural convection stability in a rectangular cavity of square section, filled with a liquid metal. These authors founded that the vertical direction of the magnetic field is most effective for the suppression of oscillations. This is in good agreement with the work of Gelfgat and Bar-Yoseph (2001).

However, when the applied magnetic field is high

or the collision frequency is low, the Hall effect plays an important role in many engineering manufacturing. Abo-Eldahab and Elbarbary (2001) studied the Hall current effects on magneto hydrodynamic free convection flow past a semi-infinite vertical plate with mass transfer. Anwar Bég *et al.* (2010) examined numerically magneto hydrodynamic viscous plasma flow in rotating porous media with Hall currents and inclined magnetic field.

Abo-Eldahab and Abd El Aziz (2004) studied the effects of Hall current and Ohmic heating on mixed convection boundary layer flow of a micropolar fluid from a rotating cone. Abo-Eldahab and Salem (2004) examined the Hall current effects on magneto hydrodynamics free convection flow of non-Newtonian power-law fluid over a stretching surface. Takhar (2006) studied unsteady free convective flow over an infinite vertical porous plate with combined effects of thermal and mass diffusion, magnetic field and Hall current. Salem and El-Aziz (2008) examined the effects of Hall currents and chemical reaction and hydromagnetic flow of a stretching vertical surface with internal heat generation/absorption. Abo-Eldahab *et al.* (2007) studied the Hall current effect on MHD mixed convection flow from an inclined continuously stretching surface with blowing/suction and internal heat generation/absorption. Shit and Halder (2012) carried out an analysis on thermal radiation and Hall current effects on MHD free convective flow and mass transfer over a stretching sheet with variable viscosity with heat generation/absorption. El-Aziz (2010) investigated the Hall effect on the boundary layer flow and heat transfer of electrically conducting fluid over a horizontal stretching surface. Recently, Aurangzaib *et al.* (2012) investigated the effect of thermal stratification on magneto hydrodynamic free convection boundary layer flow with heat and mass transfer of an electrically conducting fluid over an unsteady stretching sheet in the presence of strong magnetic field. Rana and Bhargava (2012) analyzed numerically flow and heat transfer of a nano-fluid over a nonlinearly stretching sheet. In all the above studies the researchers considered the Hall effect in the absence of nano-particles in the base fluid.

In the present work, we present a three-dimensional numerical study on the value of the Grashof number Gr , and the Aspect ratio $A=4$. Here, the combined effect on the flow structure of wall electrical conductivity and magnetic field are numerically investigated and the results are discussed within the context of Bridgman crystal growth.

2. GEOMETRY AND MATHEMATICAL MODEL

The geometry of the flow field analyses in this study is illustrated in Fig. 1. A liquid metal with a density ρ , a kinematics viscosity ν and an electrical conductivity σ , fills a rectangular cavity of dimensions $L \times H \times l$, having an aspect ratio

$A=L/H=4$, and submitted to a uniform magnetic field B_0 . The magnetic field is applied in y direction. The cavity is isothermally heated from the left vertical wall with a uniform constant temperature T_H and the right vertical with temperature T_C ($T_H > T_C$). The fluid contained in the rectangular cavity is the Mercury whose Prandtl number equal to 0.024.

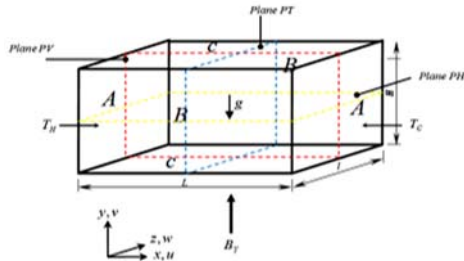


Fig. 1. The geometry of the problem.

We will refer to different cross-sections of the cavity, in order to describe both the numerical and the experimental flows. We denote by (X-Y) Plane PV, (Y-Z) Plane P T and (X-Z) Plane HP cross-sections, the planes which are perpendicular to the z, x and y-axes respectively and in addition, we indicate the coordinates of their centers. Examples of three cross-sections, centered on $x = Ax=2$, $y = 0$ and $z = 0$ can be seen in figure 1. These will commonly be referred to as the central cross-sections.

The governing equations are obtained using the following assumptions:

- Joule heating is negligible.
- Viscous dissipation is negligible.
- The induced magnetic field is negligible because $Re_m \ll 1$.
- The liquid metal is not magnetized ($\mu_m=1$).
- The liquid metal is incompressible and Newtonian.
- The Boussinesq approximation holds.

The interaction between the magnetic field and convective flow involves an induced electric current: $\vec{j} = \sigma[-\vec{\nabla}\phi + \vec{V} * \vec{B}]$

The divergence of Ohm's law $\vec{\nabla} \cdot \vec{j} = 0$ produces the equation of the electric potential:

$$\nabla^2 \phi = \vec{\nabla} \cdot (\vec{V} \times \vec{e}_B) \quad (1)$$

Whereas those of F have been obtained using the equation: $\vec{F} = \vec{j}^* * \vec{B}$

By neglecting the induced magnetic field, the dissipation and Joule heating, and the Boussinesq approximation is valid; and using H , α/H , H^2/α , ρ_0 (α/H)², αB_0 and $(T_H - T_C)$ as typical scales for lengths, velocities, time, pressure, potential, and temperature, respectively, the dimensionless governing equations for the conservation of mass, momentum and energy, together with appropriate boundary conditions in the Cartesian coordinates system (x, y, z) , are written as follows:

$$\frac{\partial U}{\partial X} + \frac{\partial V}{\partial Y} + \frac{\partial W}{\partial Z} = 0 \quad (2)$$

$$\frac{\partial U}{\partial t} + \frac{\partial(UU)}{\partial X} + \frac{\partial(VU)}{\partial Y} + \frac{\partial(WU)}{\partial Z} = -\frac{\partial P}{\partial X} + Pr \left[\frac{\partial^2 U}{\partial X^2} + \frac{\partial^2 U}{\partial Y^2} + \frac{\partial^2 U}{\partial Z^2} \right] + F_X$$

$$\frac{\partial V}{\partial t} + \frac{\partial(UV)}{\partial X} + \frac{\partial(VV)}{\partial Y} + \frac{\partial(WV)}{\partial Z} = \frac{\partial P}{\partial Y} + Pr \left[\frac{\partial^2 V}{\partial X^2} + \frac{\partial^2 V}{\partial Y^2} + \frac{\partial^2 V}{\partial Z^2} \right] + Ra.Pr.\Theta + F_Y \quad (3)$$

$$\frac{\partial W}{\partial t} + \frac{\partial(UW)}{\partial X} + \frac{\partial(VW)}{\partial Y} + \frac{\partial(WW)}{\partial Z} = \frac{\partial P}{\partial Z} + Pr \left[\frac{\partial^2 W}{\partial X^2} + \frac{\partial^2 W}{\partial Y^2} + \frac{\partial^2 W}{\partial Z^2} \right] + F_Z$$

$$\frac{\partial \Theta}{\partial t} + \frac{\partial(U\Theta)}{\partial X} + \frac{\partial(V\Theta)}{\partial Y} + \frac{\partial(W\Theta)}{\partial Z} = \left[\frac{\partial^2 \Theta}{\partial X^2} + \frac{\partial^2 \Theta}{\partial Y^2} + \frac{\partial^2 \Theta}{\partial Z^2} \right] \quad (4)$$

Where $Ra = \frac{g \beta (T_H - T_C) H^3}{\alpha \nu}$ are the

Rayleigh number, $Gr = g \beta (T_H - T_C) H^3 / \alpha^2$ is the Grashof number, $Ha = B_0 H \sqrt{\sigma / \rho \nu}$ the Hartmann number, and $Pr = \nu / \alpha$ the Prandtl number.

- Electric potential equation:

Horizontally applied magnetic field:

$$\frac{\partial^2 \phi}{\partial X^2} + \frac{\partial^2 \phi}{\partial Y^2} + \frac{\partial^2 \phi}{\partial Z^2} = \left[\frac{\partial W}{\partial Y} - \frac{\partial V}{\partial Z} \right] \quad (5-a)$$

Vertically applied magnetic field:

$$\frac{\partial^2 \phi}{\partial X^2} + \frac{\partial^2 \phi}{\partial Y^2} + \frac{\partial^2 \phi}{\partial Z^2} = \left[\frac{\partial U}{\partial Z} - \frac{\partial W}{\partial X} \right] \quad (5-b)$$

Transversally applied magnetic field:

$$\frac{\partial^2 \phi}{\partial X^2} + \frac{\partial^2 \phi}{\partial Y^2} + \frac{\partial^2 \phi}{\partial Z^2} = \left[\frac{\partial V}{\partial X} - \frac{\partial U}{\partial Y} \right] \quad (5-c)$$

Case of a horizontal magnetic field when B is applied in the x-direction, the expressions is:

$$F_X = 0; j_X = -\frac{\partial \phi}{\partial X}$$

$$F_Y = \left(-\frac{\partial \phi}{\partial Z} - V \right) . Ha^2 . Pr ; j_Y = -\frac{\partial \phi}{\partial Y} + W$$

$$F_Z = \left(\frac{\partial \phi}{\partial Y} - W \right) . Ha^2 . Pr ; j_Z = -\frac{\partial \phi}{\partial Z} - V \quad (6-a)$$

Case of a vertical magnetic field when B is applied in the y-direction, the expressions is:

$$F_X = \left(\frac{\partial \phi}{\partial Z} - U \right) . Ha^2 . Pr ; j_X = -\frac{\partial \phi}{\partial Y} - W$$

$$F_Y=0; j_Y = -\frac{\partial\varphi}{\partial Y}$$

$$F_Z=\left(-\frac{\partial\varphi}{\partial Y} - W\right).Ha^2.Pr; j_Z = -\frac{\partial\varphi}{\partial Z} + U \quad (6-b)$$

Case of a transversal magnetic field when B is applied in the z-direction, the expressions is:

$$F_X=\left(-\frac{\partial\varphi}{\partial Y} - U\right).Ha^2.Pr; j_Y = -\frac{\partial\varphi}{\partial Y} + V$$

$$F_Y=\left(\frac{\partial\varphi}{\partial X} - V\right).Ha^2.Pr; j_Y = -\frac{\partial\varphi}{\partial Y} - U$$

$$F_Z=0; j_Z = -\frac{\partial\varphi}{\partial Z} \quad (6-c)$$

The initial conditions impose that the fluid is at rest and that the temperature distribution is zero, and that the electric potential is zero everywhere in the rectangular cavity. Thus:

- At $t=0$, we have:

$$u=v=w=T=\varphi=0.$$

- At $t>0$ the boundary conditions of the dimensionless quantities (u, v, w, T and φ) are:

$$\text{At } X = 0; U = V = W = 0, \Theta = 1 \text{ and } \frac{\partial\varphi}{\partial x} = 0$$

$$\text{At } X = 4; U = V = W = 0, \Theta = 0 \text{ and } \frac{\partial\varphi}{\partial x} = 0$$

$$\text{At } Y = 0; U = V = W = 0, \frac{\partial\theta}{\partial Y} = 0 \text{ and } \frac{\partial\varphi}{\partial y} = 0$$

$$\text{At } Y = 1; U = V = W = 0, \frac{\partial\theta}{\partial Y} = 0 \text{ and } \frac{\partial\varphi}{\partial y} = 0$$

$$\text{At } Z = 0; U = V = W = 0, \frac{\partial\theta}{\partial Z} = 0 \text{ and } \frac{\partial\varphi}{\partial z} = 0$$

$$\text{At } Z = 1; U = V = W = 0, \frac{\partial\theta}{\partial Z} = 0 \text{ and } \frac{\partial\varphi}{\partial z} = 0$$

3. NUMERICAL METHOD

The equations (1-4) with the boundary conditions were solved by using the finite volume method (1980). Scalar quantities (P, T, Θ) were stored in the center of these volumes, whereas the vectorial quantities (u, v, w) are stored on the faces. For the discretization of spatial terms, a second-order central difference scheme was used for the diffusion and convection parts of the equations (2-5), and the SIMPLER algorithm was used to determine the pressure from continuity equation.

In MHD flows boundary layers different to those in ordinary hydrodynamics occur. At walls perpendicular to the magnetic field Hartmann layers of thickness $\delta_H \sim Ha^{-1}$ appear which are characterized by an exponential decay of the velocity towards the wall.

At walls parallel to the magnetic field, the so-called side layer exists, which is different in shape and

thickness ($\delta_s \sim Ha^{-1/2}$) compared to the Hartmann layers. In order to capture the Hartmann and side layers and by taking into account the fact that their thickness diminish as Ha increases ($\delta_H \sim Ha^{-1}$ and $\delta_s \sim Ha^{-1/2}$) the grid line densities have been chosen according to the value of the magnetic field B and its direction. These are given in Table 1. The increments DX, DY and DZ of the grid used are not regular. They were chosen according to geometric progressions of ratio 1.07 which permitted grid refinement near the walls; i.e. in the Hartmann and side layers where large velocity and temperature gradients exist, thus requiring a larger number of nodes.

Table 1 Meshes used in the computations

	Ha	Meshsize $N_x \times N_y \times N_z$
Nomagnetic field	0	30x30x20
y-Direction magnetic field fig.2 (b)	25	30x44x20
	50	30x64x20
	75	30x70x20
	10	30x90x20
	0	

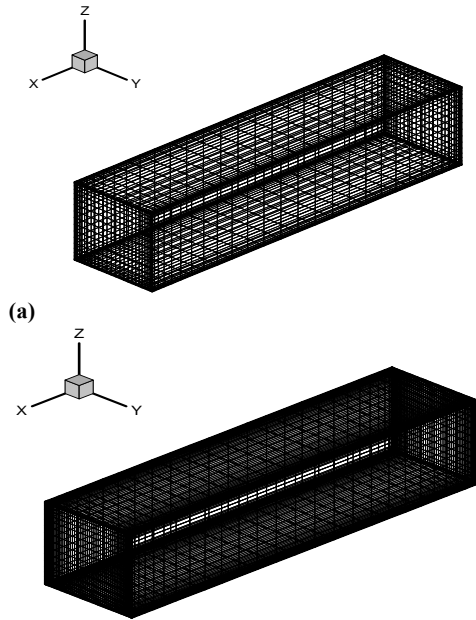
The grid used for $Ha = 0$ was chosen after performing grid independency tests. The computed average Nusselt numbers for grids finer than 30x30x20 only differ by 5×10^{-4} hence the choice of this grid fig. 2(a). Convergence of the numerical solution was obtained when the mass, momentum and energy residuals are below 10^{-4} .

The magnetic field direction y was resolved by a comparatively smaller number of points since the above-mentioned integral model was adopted for the Hartmann layers. Some simulations with no MHD effects were also performed; for these cases, a non-equispaced grid with $N_x \times N_y \times N_z = 30 \times 64 \times 20 = 38400$ nodes was used Fig.2 (b). 10000 iterations at most were needed for a complete convergence of all variables; the convergence speed was thus higher than for the quasi-2D, fully developed, problem and was only slightly affected by the conductivity of the walls, the Rayleigh number, or the Hartmann number. All simulations were run on an Intel Core Duo- 1.67 GHz computer with 2 Go RAM; each test case typically required 2 h of CPU time. These results are obtained by personal numerical code in FORTRAN software; the graphics is done by Tecplot.

3.1 Discretization Implied a General Equation of the Variable Transportation Φ

The physical area is divided into a number of finite volumes; the volume is limited by six planes, denoted by lowercase letters corresponding to their directions (e, w, n, s, t and b) relative to the central node 'P'. E, W, N, S, T and B are the centers of adjacent volumes located respectively to the East, West, North, South, upstream and downstream from that containing P. scalar quantities: pressure, temperature and electrical potential is stored finite

volume centers. As against the velocity components are located at finite volume faces. The increments Δx , ΔY , Δz and the mesh used are irregular. They were selected according to a geometric progression of 1.07, allowing a mesh refinement near the walls of the chamber where strong gradients of velocity and temperature exist.



(a) (b) Fig. 2. Mesh size, $N_x \times N_y \times N_z$ (a) No magnetic field (30x30x20) $Ha=0$. (b) y-Direction magnetic field (30x64x20) $Ha=50$.

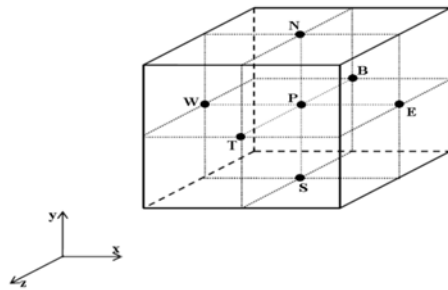
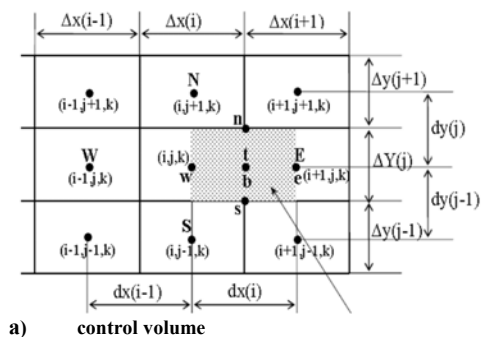
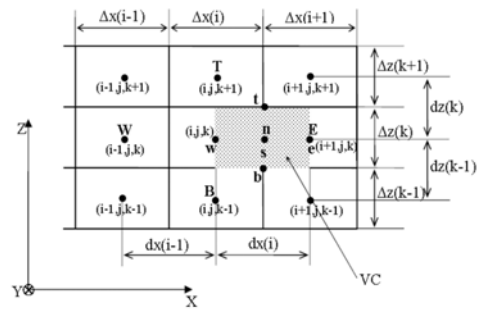


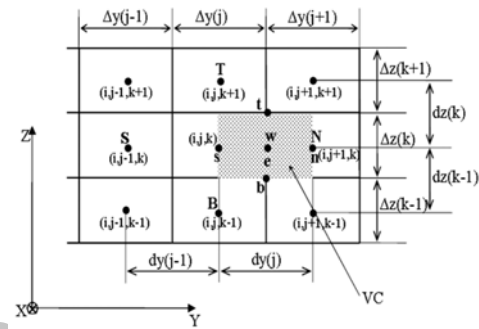
Fig. 2-1. Volume control on which the differential partial differential equations are integrated.



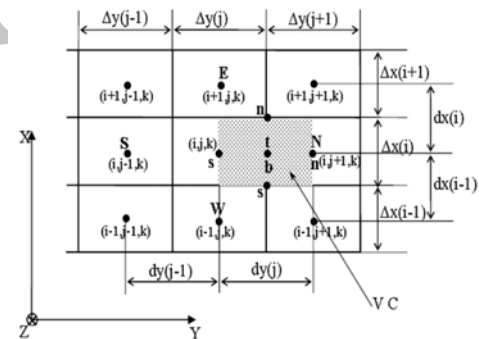
a) control volume



b) Fig. 2-2. control volume (the following equation x pulse) of interlaced mesh to the velocity component u (a) in view OXY, (b) in view OXZ.



a)



b)

Fig. 2-3. Control volume (of the next pulse equation y) of interlaced mesh to the velocity component v : (a) in view OYZ, (b) in view OYX.

The general transmission equation:

$$\frac{\partial \phi}{\partial t} + \frac{\partial (U_i \phi)}{\partial X_i} = \frac{\partial}{\partial X_i} \left(\Gamma \phi \frac{\partial \phi}{\partial X_i} \right) + S_\phi \quad (7)$$

With an incompressible fluid (or $\phi = U, V, W, \Theta$) with $j = 1, 2, 3$ (sum Index). For the dependent variable ϕ discretization equation, we integrate the general equation (7) on a volume of $\Delta X, \Delta Y, \Delta Z$ dimension control, we get:

$$A_P \phi_P = A_E \phi_E + A_W \phi_W + A_N \phi_N + A_S \phi_S + A_T \phi_T + A_B \phi_B + b \quad (8)$$

The coefficients of the equation (8) are recalled below:

$$\begin{aligned}
 A_E &= D_e A(|P_e|) + \max(-F_e, 0) \\
 A_W &= D_w A(|P_w|) + \max(F_w, 0) \\
 A_N &= D_n A(|P_n|) + \max(-F_n, 0) \\
 A_S &= D_s A(|P_s|) + \max(F_s, 0) \\
 A_T &= D_t A(|P_t|) + \max(-F_t, 0) \\
 A_B &= D_b A(|P_b|) + \max(F_b, 0) \\
 A_P &= A_E + A_W + A_N + A_S + A_T + A_B + A_P^0 \\
 b &= \left(\bar{S}_\varphi + \frac{\varphi^n}{\Delta t} \right) \Delta X \Delta Y \Delta Z, A_P^0 = \frac{\Delta X \Delta Y \Delta Z}{\Delta t}
 \end{aligned}
 \tag{8}$$

$A_E, A_W, A_N, A_S, A_T, A_B$ and A_P are the coefficients corresponding respectively to nodes East, West, North, South, front, back and A_P^0 center of the control volume; and is the coefficient of the variable to calculate the point P, at a preceding instant. b is a source term assumed to be constant in the control volume. $F_e, F_w, F_n, F_s, F_t, F_b$ and $D_e, D_w, D_n, D_s, D_t, D_b$ are respectively convective and diffusive terms the East to faces, West, North, South, the front, back. $P_e, P_w, P_n, P_s, P_t, P_b$ Designate the ratio of convective flows diffusive flow to different sides of each control volume. The coefficients $A_E, A_W, A_N, A_S, A_T, A_B$ and A_P depend on the numerical scheme selected and the number of PECLET.

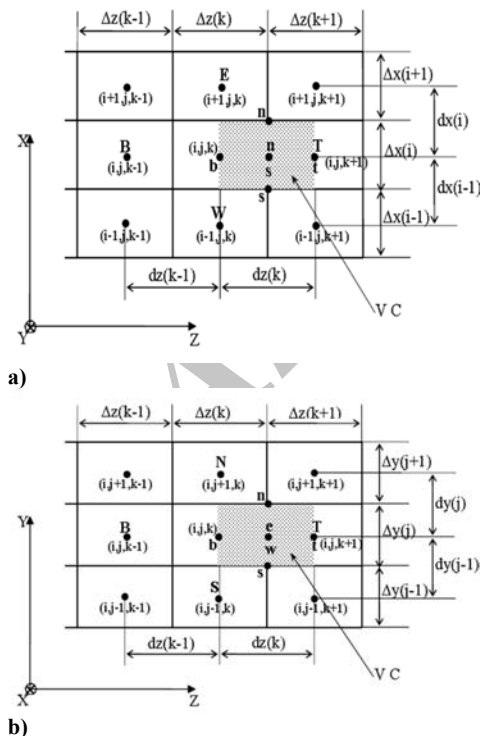


Fig. 2-4. control volume (the following equation z pulse) of interlaced mesh to the velocity component w: (a) in view OZX, (b) in view OZY.

In all our calculations on numerical scheme we

used the power law "POWER LAW" to obtain a better stability of the numerical solution. This diagram is given by the following function:

$$A(|P_i|) = \max[0.0, (1 - 0.1|P_i|)^5] \tag{9}$$

and (i = e, w, n, s, t, b).

Solving equation (7) is not easy and most direct if φ is one of the velocity components, because:

- The coefficients appearing in the discretization equation dependent variable; therefore the equation is not linear.
- The terms of sources of the equations of momentum, involve pressure gradients but we do not have equation for this variable so far.

Thanks to an algorithm called "SIMPLER Algorithm" described by Patankar, we can overcome these difficulties. This algorithm has been used in all calculations that are exposed in this works.

We have seen that the discretization replaced the partial differential equations by algebraic systems that require resolution by an iterative numerical method. This method consists of transforming a multi-dimensional discretized algebraic equation in a discrete one-dimensional equation, adding to the source of the selected dimension of the terms of other dimensions. The system of equations obtained is represented by a tri-diagonal matrix and can be solved by the Thomas algorithm.

4. RESULTS AND DISCUSSIONS

4.1. Code Validation in the Absence of a Magnetic Field:

In the absence of a magnetic field, the momentum equation (2)-(4) are solved after setting ($F_x=F_y=F_z= 0$).The results are represented graphically in Figs. 3(a)-(d).

The flow structure is shown by the velocity vectors (Fig. 3(a)) and the velocity profiles dimensionless = $(Ra*Pr)^{1/2}$ along the lines A Amid-plane (x-z) and CC mid-plane (x-y) (Figs. 3(a) and (b)). Fig. 3(a) shows that at the bottom of the cavity the flow is mainly longitudinal and is directed towards the hot wall (situated at $X = 0.0$) and at the top of the cavity the flow is directed towards the cold wall situated at $X = 1$. These boundary layers extend from the walls to the centre of the cavity, a behavior which is not common in ordinary fluids (De Vahl Davis [9]). From Figs. 3(a) and (b) one can notice that the U, V, and W profiles are linear throughout the core region extending from $X = 0.25$ to $X = 0.75$, from $Y = 0.25$ to $Y = 0.75$ and from $Z = 0.25$ to $Z = 0.75$. Comparison of Figs. 3(a) and (b) reveals the expected behavior that the flow in the vertical direction is fastest because of the buoyancy-induced acceleration experienced by fluid particles transported in this direction, the values of velocity is without units.

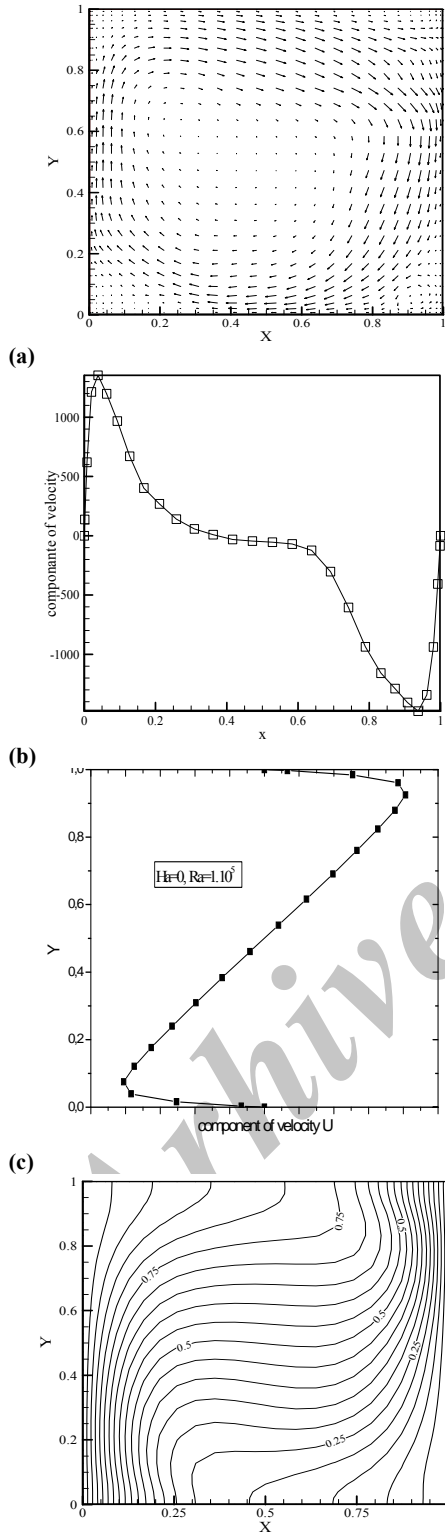


Fig. 3. (a) Velocity vector plot in plane PV for $Ha=0$ and $Ra=10^5$. (b) Distribution of velocities along line AA for $Ha=0$ and $Ra=10^5$. (c) Distribution of velocities along line CC for $Ha=0$ and $Ra=10^5$. (d) Isotherms in plane PV for $Ha=0$ and $Ra=10^5$.

A preliminary validation of the numerical method can be done, at this stage, via theoretical estimation of the magnitude of the maximum velocity, which is approximately 30 (Figs. 3(b) and (c)). One can, in effect, write, for large values of the Rayleigh number, that equilibrium exists between buoyancy forces and inertia forces, and has a value of 50. This explains the noticed distortion of the isotherms shown in Fig. 3(d).

The thermal structure of the flow is illustrated by the isotherms of Fig. 3(d) in plane PV clearly shows the formation of thermal boundary layers along the vertical walls. Here also the temperature profiles in the core region extending from $X=0.25$ to $X=0.75$ are linear. As can be noticed from Fig. 3(d) plotted using a temperature increment $\Delta\theta=0.05$ between two consecutive isotherms, the isotherms are denser on the lower part of the hot vertical wall and on the top part of the cold vertical wall. This indicates the presence of intense heat transfer across these parts of the walls. In the core region the flow is stably stratified with temperatures increasing from bottom to top. (2016).

Code verification was also done using the benchmark solution computed by De Vahl Davis and Jones [3] for natural convection in a square cavity. They present tabulated results for a range of Rayleigh numbers, $Ra=10^3, 10^4, 10^5$ and 10^6 . The quantities $U_{max}, V_{max}, Nu_{min}, Nu_{max}$ and Nu of our steady state results are compared with those obtained by their method.

The results are presented in Tables (2-5). The quantities U_{max} and V_{max} are obtained from the velocity profiles on the vertical mid-plane and on the horizontal mid-plane, respectively. The average Nusselt number is defined as:

$$\overline{Nu} \Big|_{X=0, A_x} = \int_0^1 \frac{\partial \theta}{\partial X} dY \quad (10)$$

The values of Nu_{max} and Nu_{min} are found along the hot wall. The calculated quantities show a reasonable agreement with the benchmark solution for $Ra=10^3, 10^4$ and 10^5 ; however, discretization errors cause noticeable differences (less than 5%) for $Ra=10^6$ because at this value of Rayleigh number velocity gradients in the convective terms become important, thus requiring more nodes in order to get a good resolution of the flow. These data and ours are gathered in Tables 2 -5, where the maxima (on the square cavity) and their location of the horizontal velocity component at U_{max} at $x=0$, the vertical velocity component, at $y=0$ and the Nusselt numbers Nu_{min} , and Nu_{max} , are presented. An excellent agreement is observed between the sets of data, except for the numerical values of V_{max} with respect to the data from. This is clearly due to the different choices made for uncoupling the velocity and pressure fields in the Stokes stage.

Table 2 Steady state results for $Ra=10^3$

$Ra=10^3$	Present work	Benchmark solution(1999)
U_{max}	3.646	3.649
V_{max}	3.688	3.697
Nu_{min}	0.690	0.692
Nu_{max}	1.510	1.505
\bar{Nu}	1.118	1.118

Table 3 Steady state results for $Ra=10^4$

$Ra=10^4$	Present work	Benchmark solution
U_{max}	16.152	16.178
V_{max}	19.600	19.617
Nu_{min}	0.599	0.586
Nu_{max}	3.562	3.528
\bar{Nu}	2.248	2.243

Table 4 Steady state results for $Ra=10^5$

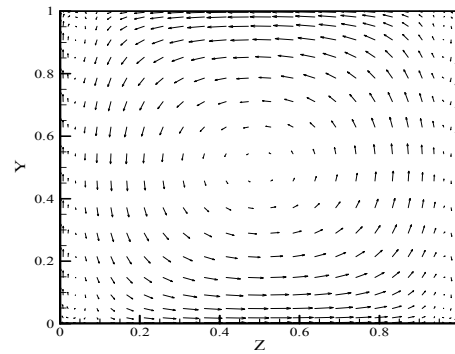
$Ra=10^5$	Present work	Benchmark solution
U_{max}	34.995	43.73
V_{max}	68.981	68.59
Nu_{min}	0.772	0.729
Nu_{max}	7.785	7.717
\bar{Nu}	4.532	4.519

Table 5 Steady state results for $Ra=10^6$

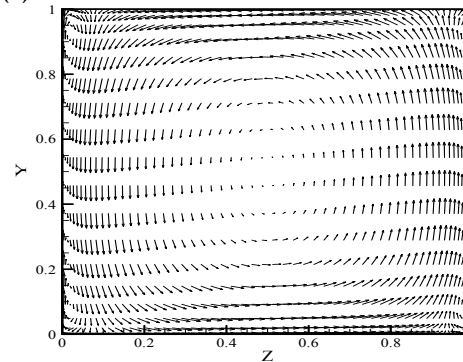
$Ra=10^6$	Present work	Benchmark solution
U_{max}	65.701	64.63
V_{max}	223.620	219.36
Nu_{min}	1.100	0.989
Nu_{max}	18.931	17.925
\bar{Nu}	8.999	8.800

4.2. Code Validation in the Presence of a Magnetic Field:

In order to give a better insight into the physics behind the change in flow pattern, sketches of the current path in plane PT corresponding to $Ha=25$ and $Ha=50$ are given, respectively, in Figs. 4(a) and (b). The Lorentz forces produced by the interaction between these currents and the applied vertical field are given, respectively, in Figs. 5(a) and (b). As can be noticed from Figs. 4, the flowing fluid generates under the action of the magnetic field, currents which are positive in the neighborhood of the top wall and negative in the neighborhood of the bottom wall. This difference in sign is due to the different directions of the fluid in contact with the top and bottom walls. Because of this difference in sign, the Lorentz force acting on the top layers of the fluid is negative (i.e. a retarding force) and that acting on the bottom layers positive (i.e. also a retarding force since the fluid flows in the negative direction towards the plane $X=0$). When the value of Ha is increased, the magnitude of Lorentz forces increases (Fig. 5) and therefore reduces the magnitude of the velocity. This provokes the damping of the flow. (2016).



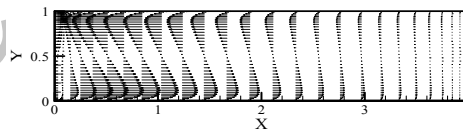
(a)



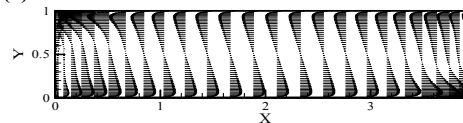
(b)

Scale : 0.44 [-]

Fig. 4. (a) Current path for $Ha=25$ in plane PT. (b) Current path for $Ha=50$ in plane PT (plane y-z).



(a)



(b)

Fig. 5. (a) Component F_x of the Lorentz force for $Ra=800$ and $Ha=25$ in plane PV. (b) Component F_x of the Lorentz force for $Ra=800$ and $Ha=50$ in plane PV (plane x-z).

4.3 Flow Fields

Fig. 6(a) and Fig. 6(b) show the velocity field of flows in the rectangular cavity for both orientations of the magnetic field. We can see that the fluid moves from the hot wall (at $x=0$) towards the cold wall (at $x=4$). As the fluid moves away from the hot wall, the magnitude of velocity increases until the fluid comes near the cold wall. In this region, the magnitude of the velocity is reduced. Both figures show a single rotating cell. At the top of the cavity, the fluid flow circulates from the hot wall towards the cold wall.

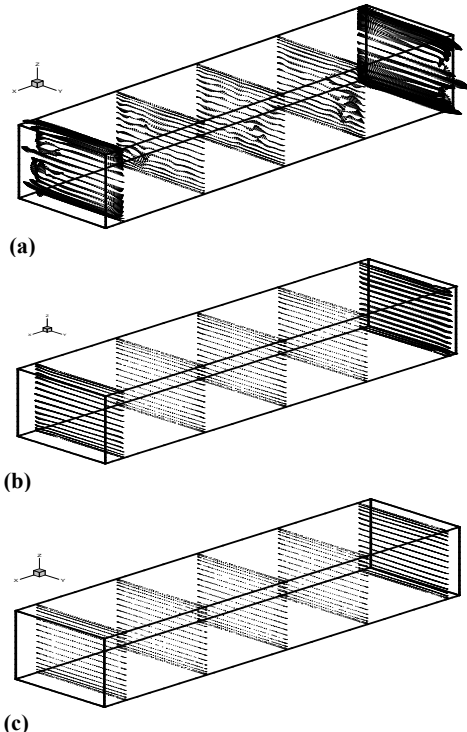


Fig. 6. Flight Path Vectors for $Gr = 10^7$ (a) $Ha=0$, (b) $Ha=50$ and (c) $Ha=100$.

4.4. Current Path and Lorentz Force

In the absence of a magnetic field the flow of mercury showed a behavior which is different from the ordinary fluid and the heat transfer coefficient which is not uniform on the cold and hot faces of the cavity Fig. 7, 8a and 9a.

Fig. 7 shows the velocity field of flows in the rectangular cavity for both orientations of the magnetic field. We can see that the fluid moves from the hot wall (at $x=0$) towards the cold wall (at $x=4$). As the fluid moves away from the hot wall, the magnitude of velocity increases until the fluid approaches the cold wall. In this region, the magnitude of the velocity is reduced. Both figures show a single rotating cell. At the top of the cavity, the fluid flow circulates from the hot wall towards the cold wall.

The magnetic field orientation according to y direction, Fig. 8 shows the distribution of the vertical component F_y of the Lorentz force in plane PT . It acts as a sink term at the proximity of the hot wall and as a source term at the proximity of the cold wall. In both cases it counteracts the buoyancy force and leads to the reduction of the velocity of the various layers of the fluid. The current distribution gives power to this force is shown in Fig.8 (a-b-c) from which one can notice that negative currents are induced near the hot wall where the flow is directed upwards and positive currents induced near the cold wall where the flow is directed downwards and that due to wall electrical insulation the iso-current lines close within the fluid.

The figures (8-10) present the densities vectors current in the plans ($x-y$, $y-z$ and $x-z$) for a vertical magnetic field. The revolving circulation of the current is created by vertical gradients of the electric potential, and this potential creates also horizontal currents close to the corners.

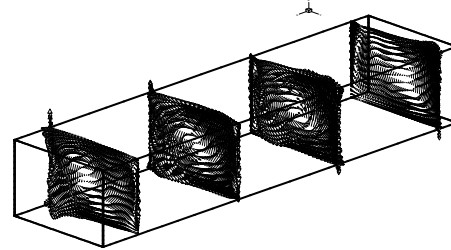


Fig. 7. Vectors of electrical current for $Gr = 10^7$ in the cavity $Ha=0$.

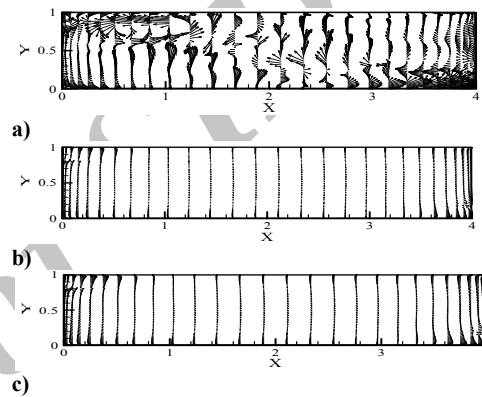


Fig. 8. Vectors of electrical current for $Gr = 10^7$ in the plans PV (Magnetic field Directed according to y): (a) $Ha=0$, (b) $Ha=50$, (c) $Ha=100$ in the plan $x-y$.

Velocity vectors, which were calculated for $Ha = 0$ and $Ha = 100$ respectively, are plotted on the central XZ -plane. The same scale was chosen to represent both flows and as a result, the projection of velocity vectors of figures 8, 9 and 10 is such that they jut over the boundaries. It is clear from this picture that the velocity field is strongly reduced in the presence of a magnetic field. At $Ha = 0$, the maximum velocity is $U_{max} = 1,13$ while for $Ha = 100$, $U_{max} = 3,45 \cdot 10^{-1}$. However, it can also be seen that the structure of the flow is strongly modified. In figure 7, dark structures can be seen in the central part of the cavity. They reflect the presence of three-dimensional secondary flows, which arise from the interaction between the recirculation flows of the two end regions. This interaction takes place in the centre of the cavity. Thus, a three-dimensional recirculation structure is generated, which is found to be at the origin of the destabilization of the flow, at larger values of the Grashof number. At $Ha = 100$, it can be seen that the central part of the flow is parallel and that the role of the end regions is simply to recirculate the fluid within the cavity. Thus, the structure of the flow is altered in the presence of a strong magnetic field, so that it becomes increasingly uniform over the length of the

cavity.

In order to understand the physical change of the flow structure, the electrical vectors current are represented in Fig. (11) for the numbers of Hartmann ($Ha=50$ and $Ha=100$). The electrical vectors current are represented in two sections inside the cavity parallel with the plan ($y-z$), and on the walls hot and cold. One can notice easily, that the direction of rotation of these vectors is anti-clockwise figures (10 (a) and (c)). The increase in the magnetic field modifies the intensity of the electrical current. In the medium of the cavity, the intensity of the current (j_y , j_x and j_z) is low compared to the walls with ($Ha=0$).

The couple (j_y and j_z) forms a closed loop of the electrical current and which guaranteed conservation of the current.

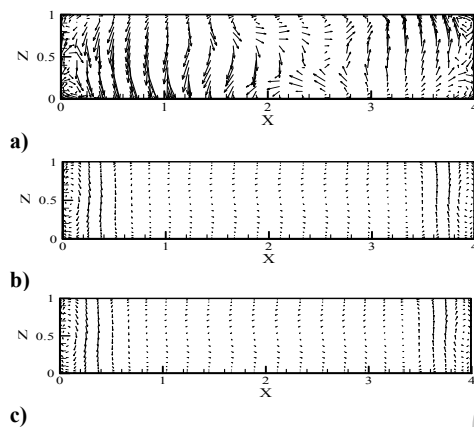


Fig. 9. Vectors of electrical current for $Gr = 10^7$ in the plans PH (Magnetic field Directed according to y): (a) $Ha=0$, (b) $Ha=50$, (c) $Ha=100$ in the plan $x-z$.

4.5. Effect on the Thermal Structure

In order to visualize the flow and the temperature distribution within the studied area, streamlines and isotherms in 3D as well as isotherms on the heating sections are respectively shown in figures 12a, 2b and 12c. It is seen that the fluid flow consists of a big and unique cell occupying the entire cavity. The fluid motion leads the heat from the active sections through the cavity. High values of the temperature are normally observed in the right-diagonally part of the enclosure (red color) and this part is organized with the augmentation for Hartmann number

The isotherms for the vertically directed magnetic field are shown in Figs. 12(a-c). Strong convection is indicated by distorted isotherms within the cavity. As the Ha is increased, thermal stratification in the core is more and more destroyed and the isotherms become more and more parallel to the horizontal walls, indicating the dominance of the conduction regime.

Also, the isotherms in the vertically oriented magnetic field are the least distorted implying the reduced convective heat transfer as shown in different plan in cavity and in $z-y$ direction.

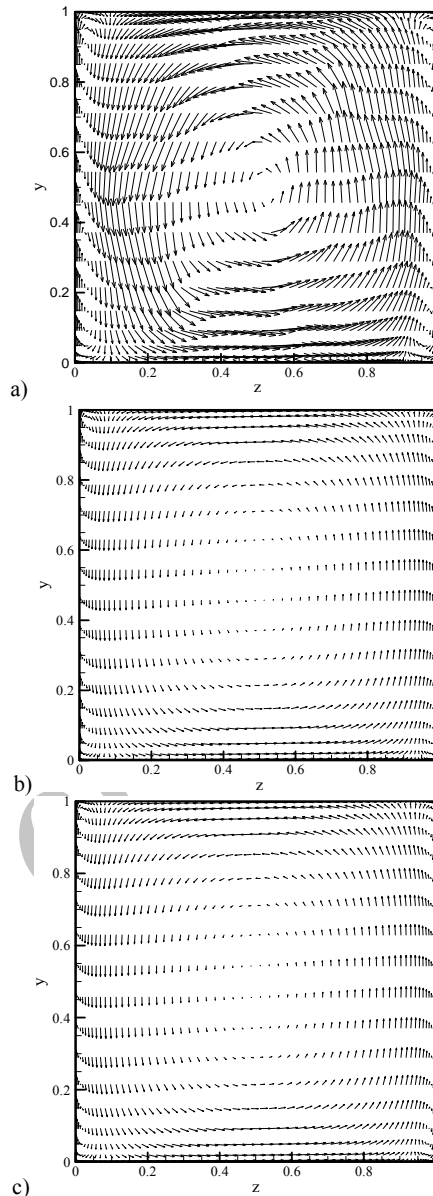


Fig. 10. Vectors of electrical current for $Gr = 10^7$ in plans PT (Magnetic field Directed according to y): (a) $Ha=0$, (b) $Ha=50$, (c) $Ha=100$ in the plan $y-z$.

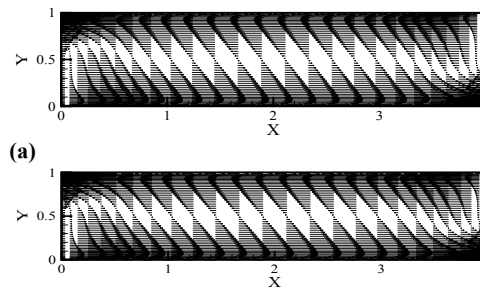


Fig. 11. Current path in plane PH for x -directed field, $Ra = 10^5$, electrically insulating walls (a) $Ha=50$ and (b) $Ha=100$.

In order to visualize the isotherms flow in the enclosure are represented on the figure (13 a, b and c) show in cavity and x-y plan. They are deformed inside the cavity because of the significant intensity of the convection appears (13 a). With the application of the magnetic field, the thermal layer in the heart of the cavity is destroyed and the isotherms become parallel to the vertical walls Figs (13 b and c) presence the magnetic field, indicating the predominance of the conductive mode.

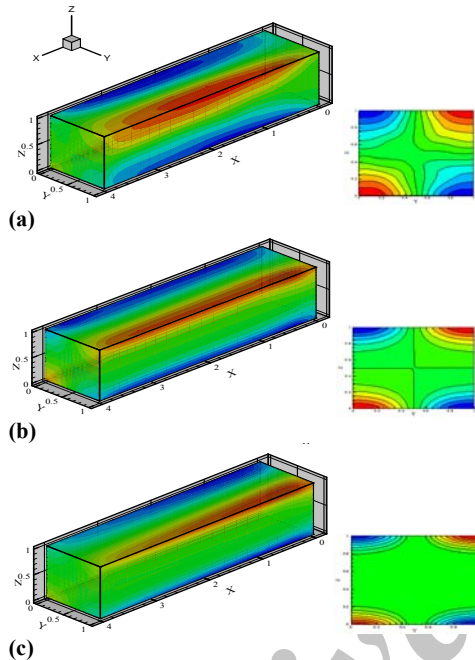


Fig. 12. Isotherms in plane PV for the vertically oriented magnetic field and $Ra=105$: (a) $Ha=25$; (b) $Ha=50$; (c) $Ha=100$.

4.6. Nusselt Number Variation

Fig. 14 shows the local Nusselt numbers, of the vertical planes at $x=2$. The contours with minus values were also drawn in dashed lines. A similar behavior of the cross-sectional velocities for the locations of the maximum local Nusselt number was also seen. For the $Ra=10^3$ and $Ha=0$ case, the peak is just located on the centerline of the cavity. In contrast, as the Hartmann number equal to zero, two peaks appear near the corners, but they are very weak and not clearly seen in the contours in Fig.14 (a). As for Figs. 14(b and c), one peak also appears but their locations do not get closer to the sidewalls or edges as the Hartmann number increases. The peaks that appeared seemed to be just getting sharpened.

Fig. 14 (c) indicate that the heat transfer across the mid-plane of $x=2$ are mainly done by advection, in contrast to the area near the vertical boundaries and with de increase the Hartmann number the heat transfer are obtained by the contours with minus values were also drawn in dashed lines.

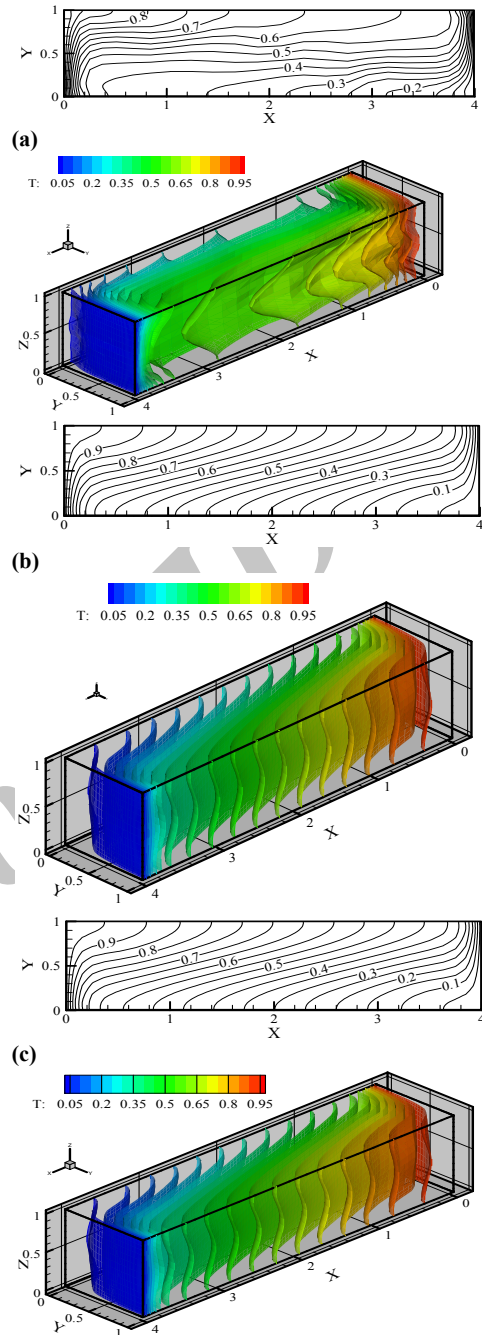


Fig. 13. Temperature Iso-surfaces, for $Gr=10^7$ (without and with magnetic field): (a) $Ha=0$ without magnetic field, (b) $Ha=50$; (c) $Ha=100$; the magnetic field is directed in the y direction.

4.7. Effect of Wall Conductivity

Figures 15(a, b and c) show that for insulated walls the surface representing the distribution of electric potential, presents variations less important than those corresponding to conducting walls. These high gradients in electric potential in the case of conducting walls are reflected,

according to Ohm's law in higher values of the electric current (Figs. 16 case1 and case4) and hence in those of the Lorentz force. Wall electrical conducting leads therefore to lower source or to higher sink terms in the momentum equations, depending on the flow direction; i.e. to an overall damping of the flow. This can be noticed through the comparison of the maximum velocities shown in Fig. 15(a). Another way for viewing the effect of magnetic field is to use the Lycoudis number Ly [3] defined by $Ly=2Ha^2/Ra^{1/2}$ and traditionally employed to correlate the heat transfer rate of free convection of a liquid metal in an external magnetic field.

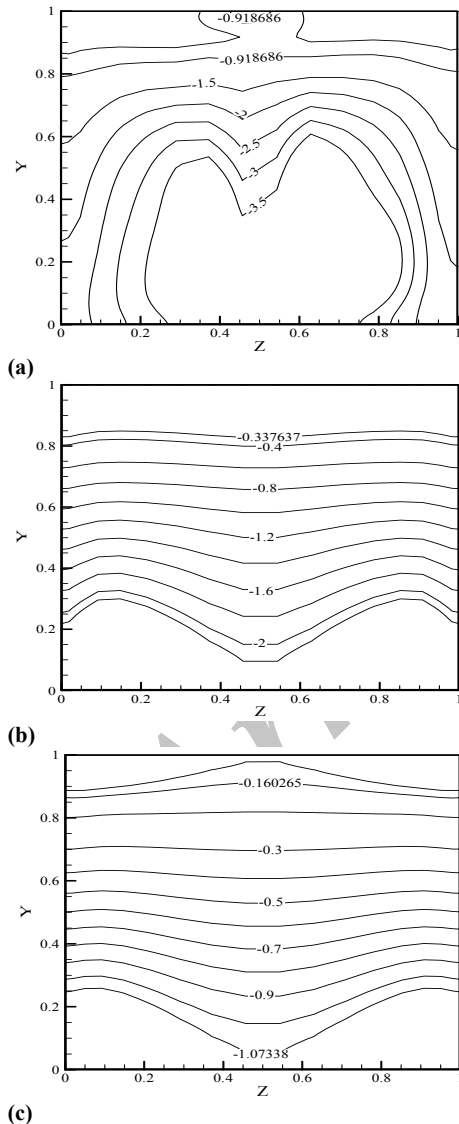


Fig. 14. Nusselt number variation of the Rayleigh number $Ra=10^5$ and the Hartmann numbers (a) $Ha=0$, (b) $Ha=50$, (c) $Ha=100$, the magnetic field is directed in the y direction.

The above conclusions that the convection is deadened better when the frontal walls ($Z=0$ and

$Z=1$) are electrically conducting. This is due to the fact that the walls electrically conducting lead to a weak source or terms raised in the equations of momentum depend on the direction of the flow, with a complete damping of the flow For example, with ($Ha=10$) the number of average Nusselt is of (2.5) without unit for case 1 is of (1.4) without unit for case 4 Fig. 15.

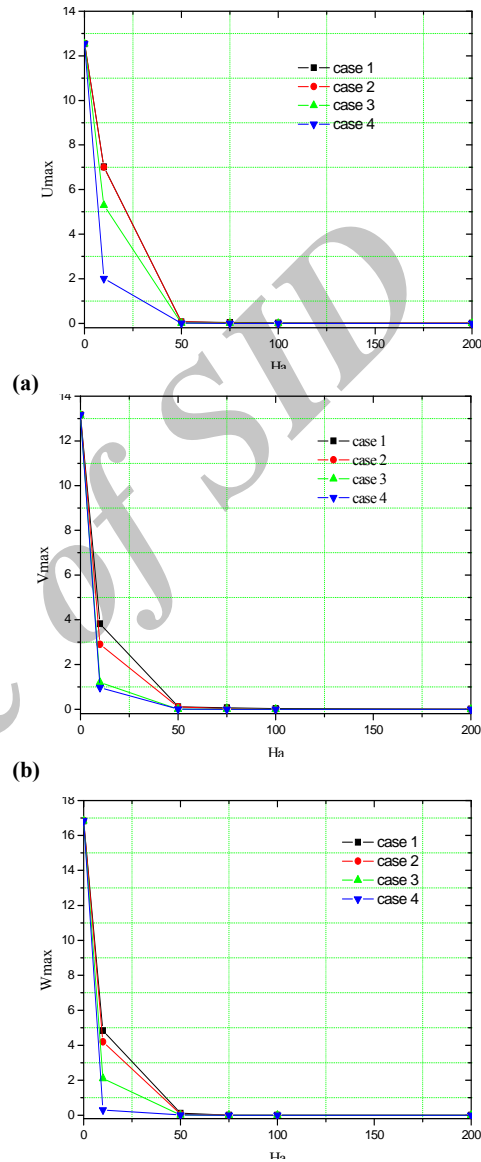


Fig. 15. Variation of $umax$, $vmax$, and $wmax$ with the Hartmann number for $Gr=10^7$ for the various cases (case 1: all the walls are electrically insulating; case 2: only the vertical walls are electrically conducting; case 3: only the horizontal walls are electrically conducting; case 4: only the frontal walls are electrically conducting) (a) $umax$, (b) $vmax$, (c) $wmax$.

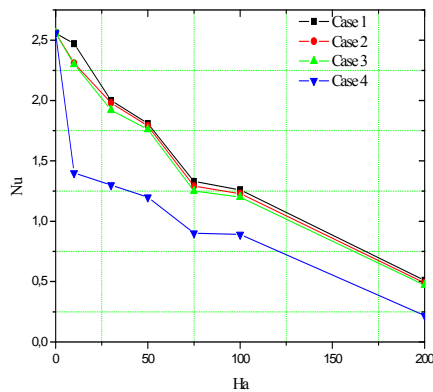


Fig. 16. Variation of average Nusselt number Nu with the Hartmann number Ha and various cases (case 1: all the walls are electrically insulating; case 2: only the vertical walls are electrically conducting; case 3: only the horizontal walls are electrically conducting; case 4: only the frontal walls are electrically conducting), for $Gr=10^7$.

5. CONCLUSION

A numerical procedure to predict the effect of electrical wall conductivity and magnetic field direction on natural convective flow in a cavity has been proposed. A good concordance between numerical results and experimental or analytical data was obtained during code validation.

In the absence of a magnetic field the flow of Mercury showed a behavior which is different from that of an ordinary fluid and a heat transfer coefficient which is not uniform on the cold and hot faces of the cavity.

When a vertical magnetic field is imposed in a relatively shallow tridimensional cavity (of aspect ratio $A=4$), the velocity profile changes from a rectangular shape ($Ha=0$) to one with a constant gradient throughout the core and peaks in the vicinity of the walls and showed Hartmann layers with varying value of the peaks in the z -direction. The side layers however have similar peaks. For a given orientation of the magnetic field, the maximum velocities in the cavity diminish as Ha is increased, implying a decrease in intensity of fluid currents circulating to-and-fro between the hot and cold walls. The orientation horizontal revealed that the one leads to the best damping of the flow. Also, electrical wall conductivity changes the Lorentz force distribution by increasing it in regions where it opposes the flow and decreasing it in the remaining regions where it is favorable to the flow: the consequence being an enhanced damping of the flow.

In conclusion, the results indicate that one can control the flow via a good choice of the strength and direction of the magnetic field, as well as of the electric conductivity of the cavity walls.

REFERENCES

- Abo-Eldahab, E. M. and A. M. Salem (2004). Hall effects on MHD free convection flow of a non Newtonian power-law fluid at a stretching surface. *International Communications in Heat and Mass Transfer* 31, 343–354.
- Abo-Eldahab, E. M., M. Abd and El. Aziz. (2004). Hall current and Ohmic heating effects on mixed convection boundary layer flow of a micropolar fluid from a rotating cone with power-law variation in surface temperature. *International Communications in Heat and Mass Transfer* 31, 751–62.
- Abo-Eldahab, E. M. and M. E. Elbarbary (2001). Hall current effect on magneto hydrodynamic free-convection flow past a semi-infinite vertical plate with mass transfer. *International Journal of Engineering Science* 39, 1641–1652.
- Abo-Eldahab, E. M., M. Abd El-Aziz., A. M. Salem and K. K. Jaber (2007). Hall current effect on MHD mixed convection flow from an inclined continuously stretching surface with blowing/suction and internal heat generation/absorption. *Applied Mathematical Modelling* 31, 1829-1846.
- Aleksandrova, S. and S. Molokov (2004). Three-dimensional buoyant convection in a rectangular cavity with differentially heated walls in a strong magnetic field. *Fluid Dynamics Research*. 35, 37-66.
- Anwar Bég, O. Lik Sim, J. Zuecoa and R. Bhargava (2010). Numerical study of magneto hydrodynamic viscous plasma flow in rotating porous media with Hall currents and inclined magnetic field influence, *Communications in Nonlinear Science and Numerical Simulation* 15, 345–359.
- Aurangzaib, A. R. M. K., N. F. Mohammad and S. Shafie (2012). Effect of thermal stratification on MHD free convection boundary layerflow with heat and mass transfer overan unsteady stretching sheet with heat source, Hall current and chemical reaction. *International Journal of Advances in Engineering Sciences and Applied Mathematics* 4, 217–225.
- Benhadid, H. H. D. (1997). Numerical study of convection in thehorizontal Bridgman configuration under the action of a constant magnetic field. Part2. Threedimensional flow. *Journal of Fluid Mechanics* 333, 57-83.
- Bessaih, R. K. and M. Marty (1999) Ph Effect of wall electrical conductivity and magnetic field orientation on liquid metal flow in a geometry similar to the horizontal Bridgman configuration for crystal growth. *International Journal of Heat and Mass Transfer*. 42, 4345-4362.
- El-Aziz, M. A. (2010). Flow and heat transfer overan unsteady stretching surface with Hall effect. *Meccanica* 45, 97

- Gelfgat, A., Y. Bar and P. Z. Yoseph (2001). The effect of an external magnetic field on oscillatory instability of effective flows in a rectangular cavity. *Physics of Fluids*. 13, 2269-2278.
- Hill, P. (1998) Crystal growth meets demands of opto devices. *Opto & Laser Europe* 56, 33-35.
- Hof, B., A. Juel and T. Mullin (2005). Magneto hydrodynamic damping of oscillations in low-Prandtl-number convection. *Journal of Fluid Mechanics* 545, 193-201.
- Juel, A., T. Mullin, H. Benhadid and D. Henry (1999). Magneto hydrodynamic convection in molten gallium. *Journal of Fluid Mechanics* 378, 97-118.
- Kherief, N. M., F. Berrahil and K. Talbi (2016). magneto-hydrodynamic flow in a two-dimensional inclined rectangular enclosure heated and cooled on adjacent walls. *Journal of Applied Fluid Mechanics*. 9, 3.
- Patankar, S. V. (1980). *Numerical Heat Transfer and Fluid Flow*. Hemisphere: Washinton DC, ch.4.
- Rana, P. and R. Bhargava (2012). Flow and heat transfer of a nanofluid over a nonlinearly stretching sheet: A numerical study. *Communications in Nonlinear Science and Numerical Simulation* 17(1), 212-226.
- Salem, A. M. and M. Abd. El-Aziz (2008). Effect of Hall currents and Chemical reaction and Hydromagnetic flow of a stretching vertical surface with internal heat generation/absorption. *Applied Mathematical Modelling* 32, 1236-1254.
- Shit, G., C. R. Haldar (2012). Combined effects of thermal radiation and Hall Currenton MHD free-convective flow and mass transfer over a stretching sheet with variable viscosity. *Journal of Applied FluidMechanics* 5(2), 113-121.
- Tagawa, T. and H. Ozoe (1997). Enhancement of heat transfer rate by application of a static magnetic field during natural convection of liquid metal in a cube. *Journal of Heat Transfer, ASME* 119, 265-271.
- Takhar, H. S., S. Roy and G. Nath (2006). Unsteady flowfree convective flow over an infinite vertical porous plate due to the combined effects of thermal and mass diffusion, magnetic field and Hall current. *Journal of Heat and Mass Transfer* 39, 823-834.
- Teng, 1., 1. Chen, S. Smith and L. Lam (2002). *FRP-Strengthened RC Structures*. Chichester, UK.: John Wiley and Sons.
- Xu, B., B. Q. Li and D. E. Stock (2006). An experimental study of thermally induced convection of molten gallium in magnetic fields *International Journal of Heat and Mass Transfer*. 42, 2009-2019.